frontiers in Materials

ORIGINAL RESEARCH
published: 31 July 2020
doi: 10.3389/fmats.2020.00242

Alloy Design and Microstructure Evolution in the $Al_xCoCrFeNi$ Alloy System Synthesized by Laser Metal Deposition

Martin Kuczyk[1,2], Liliana Kotte[1], Jörg Kaspar[1], Martina Zimmermann[1,2] and Christoph Leyens[1,2]*

[1] *Fraunhofer Institute for Material and Beam Technology IWS, Dresden, Germany,* [2] *Institute of Materials Science, Technische Universität Dresden, Dresden, Germany*

In this contribution the $Al_xCoCrFeNi$ alloy system is explored thoroughly over a wide compositional range of $x = 0.2$ to 1.5 (5 to 30 at% Al). For this alloy system compositional gradient structures were produced by laser metal deposition of pre-alloyed CoCrFeNi and elemental Al powders using an in-house developed coaxial cladding system COAXpowerline. The evolution of the microstructure with increasing Al content was analyzed in the as built as well as the homogenized condition (1350 K for 20 h). Metallographic cross sections were prepared and thoroughly analyzed by means of scanning electron microscopy, energy dispersive X-ray spectroscopy, and electron backscattered diffraction. Additionally, the evolution of the sample hardness with increasing Al contents was determined for both sample conditions. In the $Al_xCoCrFeNi$ alloy system the lattice structure as well as the sample hardness can easily be adjusted by the variation of Al. With increasing Al content a phase transition from a solid solution fcc phase toward a multiphase bcc microstructure consisting of a Fe and Cr rich solid solution bcc phase and an ordered Al and Ni rich bcc B2 phase can be observed. This is combined with an increase in sample hardness from around 200 HV up to around 500 HV in the as built condition. The compositional regions of the phase transitions for both sample conditions were compared to ab initio thermodynamic calculations done using a CALPHAD approach. For the as built condition a strong deviation from the calculated transition regime could be observed. After homogenization the experimental and calculated data are in good agreement.

Keywords: additive manufacturing, laser metal deposition, high entropy alloys, high throughput screening, microstructure

OPEN ACCESS

Edited by:
Mark L. Weaver,
The University of Alabama, United States

Reviewed by:
Sung Bo Lee,
Seoul National University, South Korea
Liang-Yu Chen,
Jiangsu University of Science and Technology, China

****Correspondence:***
Martin Kuczyk
martin.kuczyk@iws.fraunhofer.de

Specialty section:
This article was submitted to Structural Materials, a section of the journal Frontiers in Materials

Received: *29 April 2020*
Accepted: *01 July 2020*
Published: *31 July 2020*

Citation:
Kuczyk M, Kotte L, Kaspar J, Zimmermann M and Leyens C (2020) Alloy Design and Microstructure Evolution in the $Al_xCoCrFeNi$ Alloy System Synthesized by Laser Metal Deposition. Front. Mater. 7:242. doi: 10.3389/fmats.2020.00242

INTRODUCTION

In 2004 Yeh et al. (2004) and Cantor et al. (2004) suggested a new group of alloys, the so called high entropy alloys (HEA). Those alloys are usually comprized of five or more metals in near equimolar ratio to each other which maximizes their configurational entropy, hence the name high entropy alloy. The microstructure of those alloys usually consists of simple solid solution fcc (e.g., Cantor alloy and its derivates) or bcc phases (Senkov alloys and derivates). Numerous

works showed that HEA demonstrate promising mechanical as well as functional properties (Miracle and Senkov, 2017).

With the introduction of HEAs and in the further sense the introduction of compositionally complex alloys (CCAs)—which are derived by softening the condition of near equal ratio of the alloyed metals—a shear infinite space of possible interesting sample compositions open up. To explore this vast space of sample compositions, the development and use of effective high throughput screening strategies becomes more and more important (Marshal et al., 2017; Li et al., 2018). Amongst those methods additive manufacturing of samples by laser metal deposition (LMD) appears very promising. The fabrication by LMD is a very suitable manufacturing process for this group of alloys. It has already been established in several industrial branches with the purpose of coating, part refurbishment, but also for the manufacturing of functional 3D components (Leino et al., 2016). LMD is suitable for a broad spectrum of metals (e.g., Fe, Ni, Ti, or Co based alloys). By combining several powder feeders a variation of the composition within the manufactured structure is feasible and therefore well suited for the exploration and development of new material systems (Brueckner et al., 2018; Gwalani et al., 2019). Moreover the typically high cooling rates (10^3–10^5 Ks^{-1}) achieved during LMD are advantageous for a significant non-equilibrium solute trapping effect which prevents the segregation of components with differing melting points and counteracts the limitations associated with low solubility (Xiang et al., 2019). In addition, the deposition by LMD can be guided by ab initio thermodynamic calculations which help identifying interesting compositional regions (Haase et al., 2017).

The vast compositional space of HEAs and CCAs, which cannot be dealt with here, has been classified into seven alloy families (Miracle and Senkov, 2017). The group of 3d transition metals has been by far the most widely studied alloy family. Within this alloy family the $Al_xCoCrFeNi$ alloy system has been of particular interest over the past years. These alloys are thought to possess considerable potential for high-temperature structural applications because of their high strength and excellent corrosion resistance (Lim et al., 2017; Mohanty et al., 2019). Usually $Al_xCoCrFeNi$ alloys are manufactured by the conventional melting and casting route and the microstructure can easily be adjusted by the variation of the overall Al content. With the addition of Al the lattice structure transforms from a solid solution fcc phase to a dual phase bcc microstructure consisting of a Fe and Cr rich solid solution bcc (A2) and an Al and Ni rich ordered bcc B2 phase (Kao et al., 2009; Wang et al., 2012). The formation of the dual A2 + B2 bcc phases has been attributed to a spinodal decomposition process (Manzoni et al., 2013). In the as cast condition this transition takes place in the compositional range from $0.4 \leq x \leq 1.0$ (8–20 at% Al). With the addition of Al ($0 \leq x \leq 1.2$) and alongside the transition from fcc to bcc microstructure, the hardness of the alloy increases from about 120 HV to about 500 HV (Kao et al., 2009). Different studies indicate that the as cast microstructures of the Al-rich ($x \geq 1$) alloys are not stable at elevated temperatures (Wang et al., 2014; Munitz et al., 2016; Meshi et al., 2019). At temperatures above 923 K the dual A2 + B2 bcc structure decomposes into B2 + fcc + σ phase. Above 1250 K the σ phase dissolves leading to a mixture of A2 + B2 + fcc phases.

In 2015, for the first time additive manufacturing of AlCoCrFeNi was demonstrated by selective electron beam melting (SEBM; Fujieda et al., 2015) and laser engineered net shaping (LENS; Kunce et al., 2015). Since then other additive manufacturing methods like LMD (Wang et al., 2017), selective laser melting (SLM; Niu et al., 2019), and binder jetting (Karlsson et al., 2019a) have been utilized to fabricate the equimolar AlCoCrFeNi alloy. Generally, within the $Al_xCoCrFeNi$ alloy system the work on additive manufacturing mainly concentrates on the equimolar AlCoCrFeNi composition. Similarly to conventionally cast samples additively manufactured AlCoCrFeNi mostly consists of a fine modulated structure of A2 + B2 bcc phases (Kunce et al., 2015; Wang et al., 2017). Only the SEBM fabricated AlCoCrFeNi samples additionally showed some minor amount of fcc phase, which was attributed to the process induced preheating (Fujieda et al., 2015). The dissimilar temperature regimes of the fabrication methods also led to different hardness values ranging from about 400 HV for SEBM samples (Shiratori et al., 2016) to about 600 HV in SLM samples (Niu et al., 2019).

Very recently it was demonstrated that LMD provides a suitable methodology for the production of compositionally graded $Al_xCoCrFeNi$ alloys (Gwalani et al., 2019) and for the high throughput screening of different alloy compositions (Li et al., 2018). The aim of the present study is to combine these two approaches and develop LMD as an effective tool for the high throughput screening of HEAs/CCAs using the $Al_xCoCrFeNi$ alloy system as an example. It will be shown that by utilizing LMD for the deposition of gradient structures the composition can be controlled sufficiently well in order to generate samples exhibiting a wide range of compositions while being deposited in one single built process. With the use of large area energy dispersive X-ray spectroscopy (EDS) and hardness line profiles over the full build height the transitional region can be characterized both sufficiently as well as efficiently. Furthermore, the microstructures within the transitional region will be analyzed in detail using scanning electron microscopy (SEM), EDS, and electron backscattered diffraction (EBSD).

AB INITIO THERMODYNAMIC CALCULATIONS

Ab initio thermodynamic calculations were done to estimate interesting compositional regions and compare the experimental results with the current understanding of the analyzed alloy system by means of the CALPHAD (CAlculation of PHase Diagrams) method. The calculations were based on databases derived from data of lower ordered systems such as binary and ternary phase diagrams as well as experimental data derived from X-ray diffraction (XRD), transmission electron microscopy (TEM), calorimetric measurements, and others. In this study the calculations were executed using ThermoCalc and the TCNi7 database. This database was optimized for calculations on Ni based alloys. However, it will be shown that the database can also

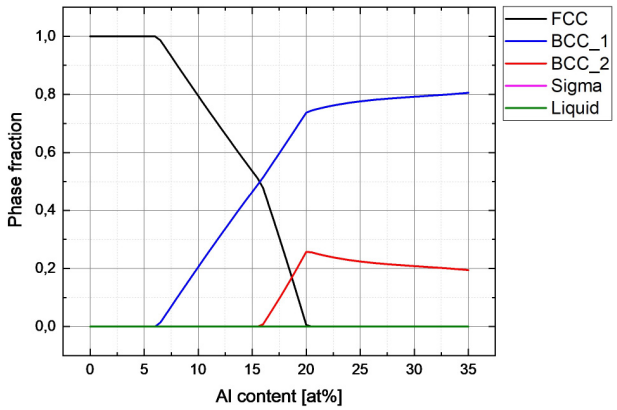

FIGURE 1 | CALPHAD calculation of the expected phase composition in the $Al_xCoCrFeNi$ alloy system at 1350 K in dependence on the Al content.

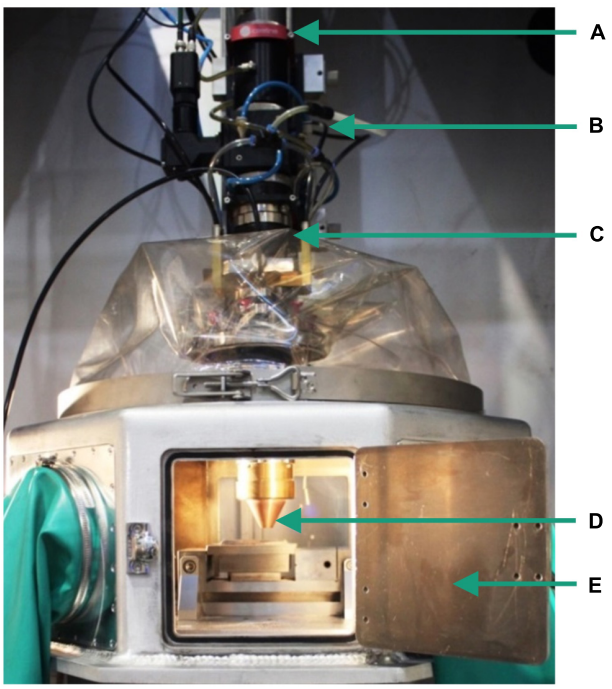

FIGURE 2 | Laser Metal Deposition (LMD) test assembly: **(A)** fiber plug; Laser LDM4000-100, Laserline GmbH; **(B)** Powder inlets; **(C)** OTS-2-optic with laser-focus of 3.8 mm; **(D)** Powder-nozzle COAXpowerline with powder-focus of 1.9–2.2 mm; and **(E)** Shielding gas chamber with Ar (O_2 < 20 ppm).

be used for the HEA material system and allows a reasonable estimation on the desired phase system.

Figure 1 summarizes the results of the CALPHAD calculations. The diagram shows the phase composition as a function of the Al content in at% near the solidification temperature at 1350 K. With increasing Al content a change in phase composition was observed. Up to an overall Al content of 5 at% the microstructure only consisted of the solid solution fcc phase. Exceeding 5 at% Al content a second phase with bcc structure denoted bcc1 appeared. Above 15 at% Al content a second bcc phase, denoted as bcc2, evolved. With increasing Al content the phase fraction of the fcc phase decreases in favor of the two bcc phases. Exceeding an Al content of 20 at% the solid solution fcc phase completely vanishes leading to a structure of mainly bcc1 and minor bcc2. Based on these calculations the interesting compositional range for the LMD experiments was set to the range from 5 to 30 at% Al content. In this region the phase transformation behavior of the LMD samples was thoroughly studied.

EXPERIMENTAL DETAILS

Two powders were used for the deposition of the gradient structures: a pre-alloyed and atomized CoCrFeNi powder with particle sizes between 45 and 90 μm (produced by Nanoval GmbH, Germany) and pure Al powder with particle sizes between 63 and 150 μm (produced by Ecka Granules, Austria). Samples of the two powders were analyzed by SEM and EDS.

The LMD experiments were carried out using the cladding nozzle COAXpowerline developed at Fraunhofer IWS. This nozzle is designed as a coaxial ring with a powder focus diameter of 1.9 to 2.2 mm. The size of the powder focus diameter was determined by the powder feed rate and its carrier gas volume flow. LMD took place in an Ar atmosphere at a working distance (distance between substrate and nozzle tip) of 13 mm. The argon atmosphere was generated in an in-house developed shielding gas chamber, having a slight overpressure of 200 mbar and a residual oxygen content of 20 ppm. A laser spot diameter of 3.81 mm being significantly larger than the diameter of the powder spot was applied for optimum powder utilization. The powder was introduced into the nozzle by four evenly distributed powder inlets. A powder distributor was positioned in front of the powder inlets in which the two base powders are fed and evenly mixed. A 4 kW diode laser from Laserline GmbH was utilized in the LMD process. The applied laser equipment is shown in **Figure 2**. In order to build up gradual compositional changes with respect to the Al content, a methodology similar to the one described by Gwalani et al. (2019) was deployed. However, in our double powder feeder arrangement, instead of $Al_{0.3}CoCrFeNi$ and $Al_{0.7}CoCrFeNi$ we used Al in one hopper and pre-alloyed CoCrFeNi in the second hopper. This development allowed to control the flow rate of both powders with high accuracy

TABLE 1 | Powder feed rate of the two powders for the three cladded gradient structures.

	Powder feed rate in g/min		Powder feed rate in g/min		Powder feed rate in g/min	
Layers	**CoCrFeNi**	**Al**	**CoCrFeNi**	**Al**	**CoCrFeNi**	**Al**
1.–3.	19.5	0.5	19.5	0.5	19.0	1.0
4.–6.	19.0	1.0	18.4	1.6	17.8	2.2
7.–9.	18.4	1.5	17.3	2.7	16.6	3.4
System	5/10/15 at% Al		5/15/25 at% Al		10/20/30 at% Al	

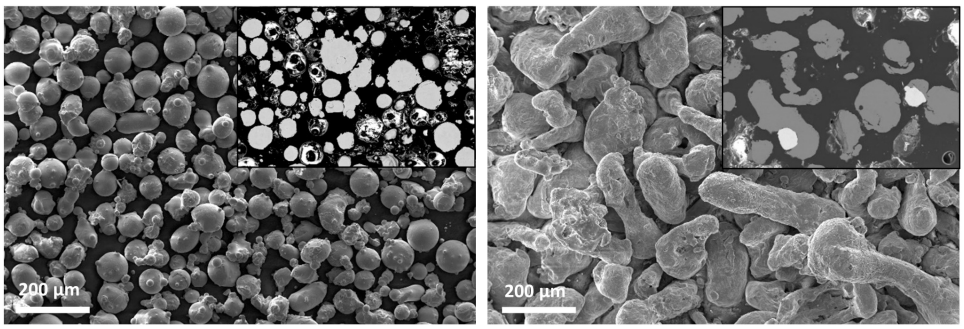

FIGURE 3 | SEM images of the used powders and powder cross sections; CoCrFeNi powder (left); Al powder (right).

TABLE 2 | Chemical composition (EDS measurements) of the used powders in at%.

	Co	Cr	Fe	Ni
CoCrFeNi	25.2	26.1	25.4	23.3
	Al	**O**		
Al	98.8	1.2		

and moreover to evenly mix the two powders in the powder distributor. Utilizing this a smooth compositional gradient was realized and the Al content was varied over a large range from 0 to 30 at% in only one gradient structure.

The cladded gradient structures were composed of nine individual unidirectional welded layers. Stainless steel 1.4301 plates of 10 mm thickness were used as substrate material. The powder feed rates of the CoCrFeNi and Al powders were varied as described in **Table 1** to produce three different gradient structures. The total powder feed rate was kept at a constant level of 20 g/min for all three samples. All samples were welded with a laser power of 1700 W and a process velocity of 600 mm/min. The gradient structures produced that way are hereby referred to as the as built sample condition.

To study the phase composition at near thermal equilibrium the laser cladded samples were subjected to a homogenization heat treatment. The samples were homogenized for 20 h at 1350 K under Ar atmosphere followed by cooling in the oven back to room temperature. The temperature range and duration were chosen on the basis of work on the same material system found in literature (Kao et al., 2009; Karlsson et al., 2019a). Those samples are hereby referred to as the heat treated or homogenized sample condition.

For the microstructural investigations the cladded samples were cut and mounted using a cold mounting epoxy resin. The samples were ground with SiC abrasive paper, wet-polished using a diamond polishing suspension, and finally vibratory polished for multiple hours using Al and Si oxide polishing suspensions. For light microscopic investigations the samples were etched using a V2A etching solution consisting of 200 ml H_20, 200 ml HCl (32%), 20 ml HNO_3 (65%), and 0.6 ml of etching additives.

Detailed microstructural investigations on polished samples were carried out in a JEOL JSM-7800F field emission SEM. EDS and EBSD analysis was carried out using an Oxford X-Max EDS detector and a NordlysNano EBSD detector as well as the Aztec data acquisition software. Additionally, the sample hardness was measured using a LM247 AT Vickers microhardness tester by LECO and a load of 0.1 kg.

RESULTS

Powder Analysis

Figure 3 shows SEM images of the used pre-alloyed CoCrFeNi powder and the elemental Al powder as well as cross sections of both powders. The pre-alloyed CoCrFeNi powder mostly contained spherical particles with a small amount of satellites as well as broken and remelted particles. The average particle diameter was about 70 µm. The chemical composition of the powder is shown in **Table 2**. It was derived from EDS data on powder cross sections. Only small deviations from the desired equimolar ratio of the four elements were detected with a slight deficit in Ni content in particular. The Al powder mostly consisted of irregular shaped elongated particles with a minor

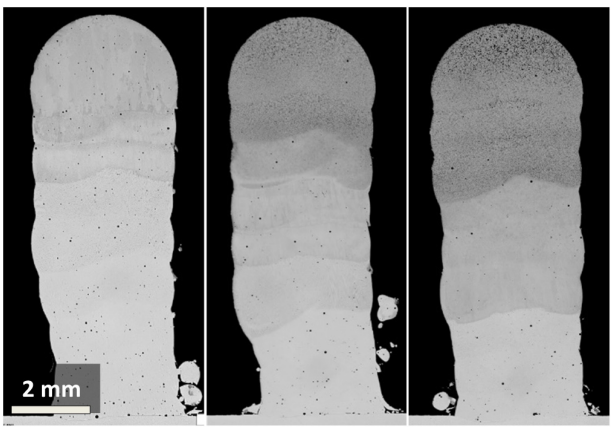

FIGURE 4 | Light microscopic images of the etched as built gradient structures; 5/10/15 at% Al (left); 5/15/25 at% Al (middle); and 10/20/30 at% Al (right).

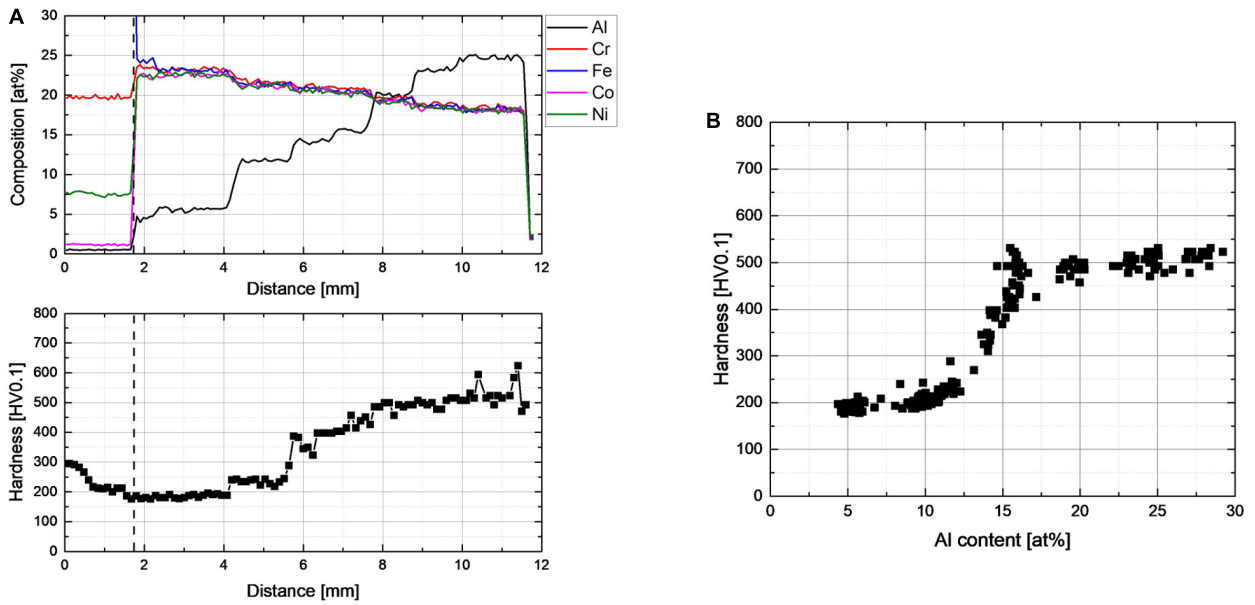

FIGURE 5 | Chemical composition and hardness of the 5/15/25 at% Al as built gradient structure **(A)**; hardness as a function of Al content derived from all three as built gradient structures **(B)**.

axis length between 63 and 150 μm (derived from manufacturer data) and a major axis length up to 300 to 400 μm. Some Ni and Fe rich foreign particles were found within the powder sample. However, no problems in powder feeding and mixing occurred during LMD.

Analysis of the as Built Sample Condition

Light microscopic images of the three different gradient samples in the as built state (**Figure 4**) revealed the nine singular layers of the cladded structures. Each gradient structure was about 4 mm wide and had a height of about 10 mm. Some larger oxide filled pores were identified in the cross sections but no major cracking occurred. Generally, for each of the three stacks, three regions each containing three layers with similar structure and color could be visualized, which is in accordance with the intended and adjusted compositions displayed in **Table 1**. However, due to dilution with the substrate and some intermixing between the individual layers during melting some deviations from the intended chemical composition developed, especially in the transition layers of the three regions. With regard to the screening approach this effect was rather regarded as an advantage. Instead of the intended three different compositions actually five or six different compositions were established in each gradient structure. For all three cladded gradient structures the chemical composition and hardness was determined. As a representative example **Figure 5A** shows the chemical composition and hardness for the gradient structure with 5, 15, and 25 at% Al. Already for this example the comparison of chemical composition and hardness illustrates how strongly the Al content defines the alloys hardness. In **Figure 5B** the hardness measurements on all three gradients are summarized and plotted against the Al content. Up to an Al content of about 10 at% the hardness remained constant at a low level of about 200 HV. In between 10 and 15 at% overall Al content the hardness rapidly increased up to about 500 HV. For Al contents of more than 15 at% the hardness no longer increased but remained at a nearly constant value of 500 HV. The change in hardness in dependence of the Al content correlated well with the change in phase composition from single phase fcc to dual phase bcc as can be seen in **Figure 6** and **Table 3**, respectively. Studying the three gradient samples over the range of 5–25 at% Al content, five major types of microstructures were identified.

Sample position 1 displays a single phase fcc solid solution microstructure with an overall Al content of about 5.0 at% and a hardness of about 200 HV. With increasing Al content more phases started to appear as can be seen at sample position 2 with an overall Al content of about 10.6 at%. Additionally to the previously mentioned fcc phase, a dual and fine-scaled mix of phases, containing more Al than the fcc phase, was found at the interdendritic sites of the microstructure. Further EDS and EBSD analysis which is displayed in **Figure 7** showed that both of these phases exhibit a bcc structure. Furthermore it is worth mentioning that one of the two bcc phases contained more Al than the other. Due to limitations of the EBSD measurements further separation of the two bcc phases was not possible. However, based on the work of Kuwabara et al. (2018) and Wang et al. (2014) it was concluded that this Al rich phase is an ordered bcc B2 phase and the second phase is the solid solution bcc A2 phase. This dual mix of phases will further be referred to as bcc*. The fraction of bcc* rapidly increased with increasing Al content which is displayed at sample positions 3 and 4 which represent an overall Al content of 13.04 at% and 13.4 at%, respectively. This increase in bcc* phase fraction correlated well with the rapid increase in sample hardness between 10 and

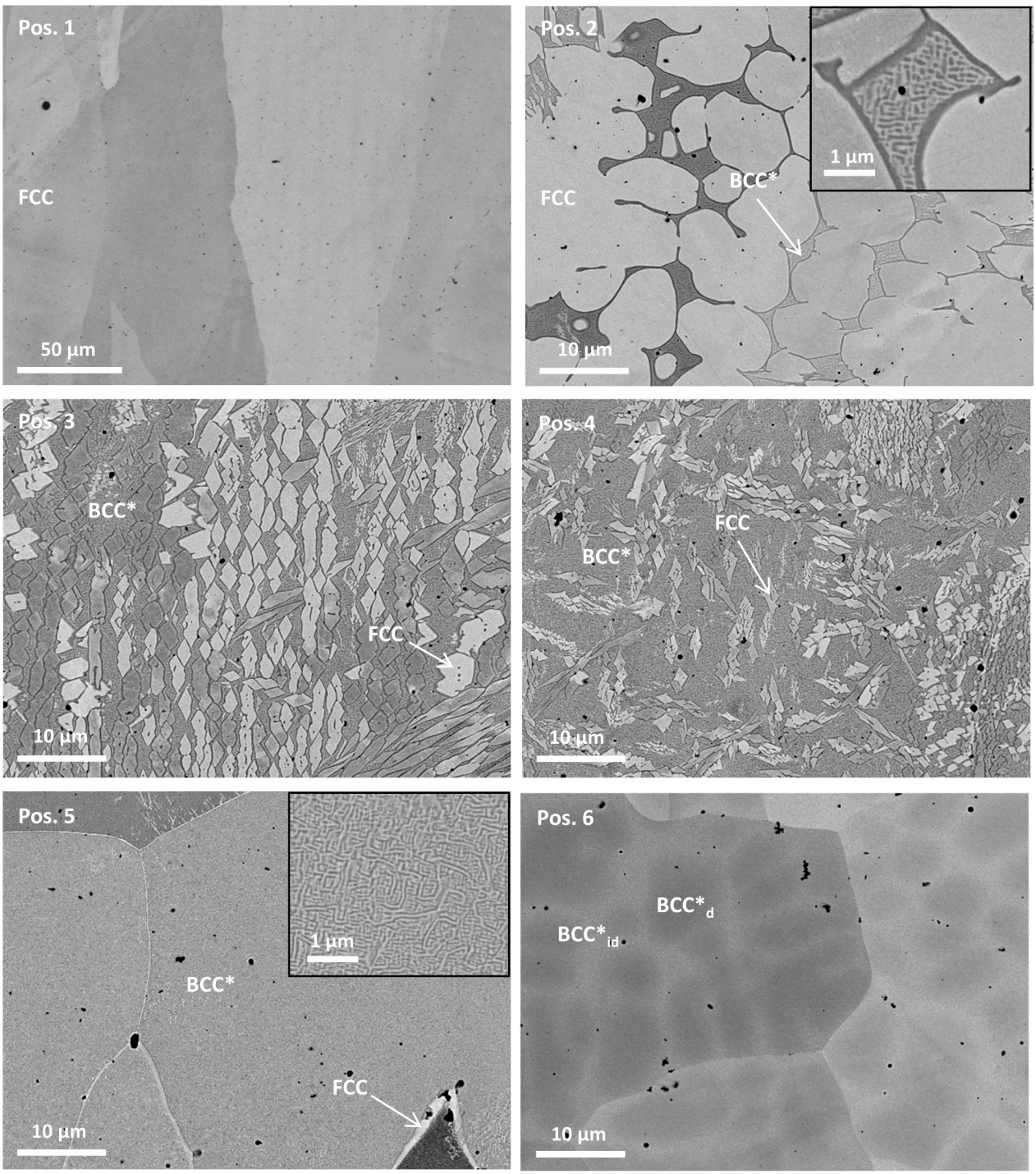

FIGURE 6 | SEM images of the major microstructures of the as built samples with increasing Al content derived from all three cladded gradients: Pos. 1 at 5.0 at% Al, Pos. 2 at 10.6 at% Al, Pos. 3 at 13.0 at% Al, Pos. 4 at 13.4 at% Al, Pos. 5 at 14.2 at% Al, and Pos. 6 at 25.8 at% Al.

15 at% overall Al content. The microstructure at sample position 5 with an overall Al content of 14.2 at% was mostly dominated by bcc* phases showing only some residual fcc phase at the grain boundaries. This is visualized in more detail by the EDS and EBSD measurements displayed in **Figure 7**. In **Figure 6** the detail inlet of the SEM micrograph at position 5 demonstrates the typical very fine-scale dual B2/A2 phase arrangement of bcc*.

At sample position 6 and an overall Al content of 25.8 at% no more residual fcc phase was found and the microstructure fully consisted of bcc* phase mixture. However, besides the

TABLE 3 | Representative EDS analysis of the major microstructures of the as-built samples (at%).

Pos.	Area	Al	Cr	Fe	Co	Ni
1	Overall	5.0	20.6	23.8	24.0	26.7
	fcc	5.0	***20.6***	***23.8***	***24.0***	***26.7***
2	Overall	10.6	19.1	21.4	22.8	26.1
	fcc	8.9	***19.0***	***22.9***	***24.3***	***24.8***
	bcc*	***14.1***	22.1	18.0	20.4	25.4
3	Overall	13.0	18.7	21.0	22.2	25.2
	fcc	9.5	***19.2***	***22.7***	***23.3***	***25.3***
	bcc*	***14.4***	20.1	20.0	21.2	24.3
4	Overall	13.4	18.6	20.9	22.0	25.2
	fcc	9.4	***19.3***	***23.0***	***23.0***	***25.2***
	bcc*	***14.2***	20.8	20.1	21.2	23.8
5	Overall	14.2	18.8	20.1	21.8	25.0
	fcc	-	–	–	–	–
	bcc*	***14.2***	18.8	20.1	21.8	25.0
6	Overall	25.8	15.0	16.6	19.9	22.6
	bcc^*_d	***30.3***	10.9	13.6	19.9	***25.3***
	bcc^*_{id}	20.9	***21.9***	***20.8***	18.9	17.5

The bold values indicate differences in phase composition.

typical grain structure a very fine dendritic structure evolved. The dendritic microstructure is composed of Al rich cores (bcc^*_d) and Cr and Fe rich inter-dendritic areas (bcc^*_{id}). From the observed elemental partitioning it was concluded that the dendrite cores mainly consisted of the bcc B2 phase, whereas the inter-dendritic areas exhibited a fine-scale dual B2/A2 phase arrangement similar to position 5. At this high Al content the sample hardness remained at its peak of about 500 HV.

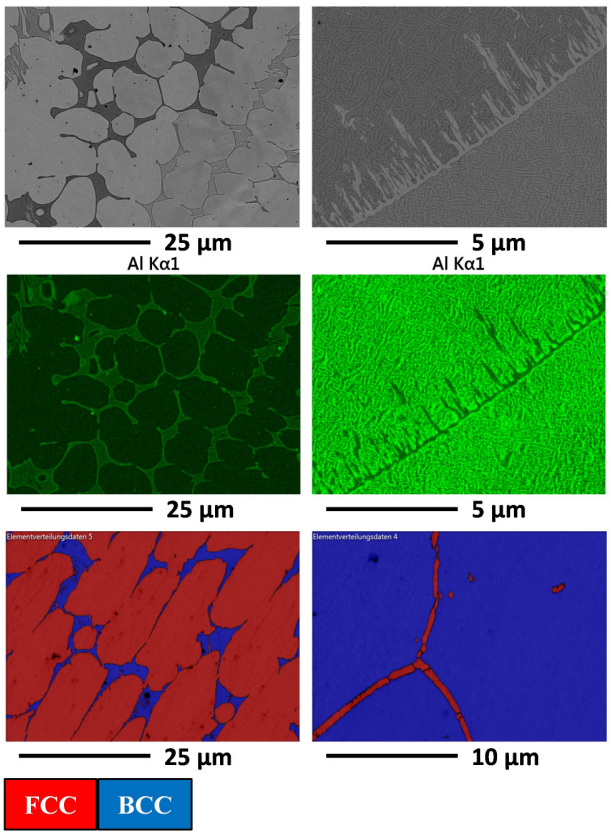

FIGURE 7 | EDS Al maps and EBSD phase maps of sample positions 2 (left) and 5 (right).

Analysis of the Heat Treated Sample Condition

After the homogenizing heat treatment at 1350 K for 20 h the sample hardness and chemical composition were determined for all three gradient structures in the same way as for the as built samples. In **Figure 8** this is shown exemplarily for the 5/15/25 at% Al gradient. In this condition the hardness stayed at 200 HV up to an overall Al content of about 5 at%. In the range from 5 to 18 at% overall Al content the sample hardness increased to its maximum of 700 HV. In the wide range from 5 to 16 at% overall Al content there was only a moderate increase in hardness to 400 HV. However, above 16 at% overall Al content the hardness rapidly jumped to 700 HV. It is worth noting that when the overall Al content exceeded about 20 at%, the hardness dropped to a constant level of about 500 HV, i.e., the same value as in the as built state. Likewise, in the heat treated condition, the change in hardness correlated with a change in microstructure from single phase fcc to dual phase bcc with increasing Al content. This is exemplarily shown in **Figure 9** and **Table 4**, respectively. Over the whole gradient structures five different types of microstructures could be distinguished.

Sample position 1, representing an overall Al content of about 4.8 at% and a hardness of 200 HV, displays a fully solid solution fcc microstructure. Hence, at this alloy composition, the heat treatment did not lead to any structural modifications. At an overall Al content of about 10.4 at% and a hardness of about 280 HV (position 2) additionally to the fcc matrix a small amount of an Al and Ni rich bcc phase was identified. Because of its composition and in accordance to Wang et al. (2014) and Kuwabara et al. (2018) this phase was assumed to be the ordered bcc B2 phase. It should be noted, that in contrast to the as built state no bcc solid solution A2 phase was found at this composition. With increasing Al content the amount of bcc B2 phase increased at the expense of the fcc solid solution phase (position 3). Consequently, the moderate hardness increase in this range of Al content was caused by the increase in bcc B2 phase content. Starting from an overall Al content of 16 at% a third phase could clearly be distinguished leading to a rather complex microstructure. Sample position 4 with an overall Al content of 17.5 at% and a hardness of 700 HV displays such a microstructure (**Figures 9**, **10**). Within the grains it consisted of a mixture of the Al and Ni rich bcc B2 phase and a Fe and Cr rich bcc solid solution A2 (bcc2). Additionally, the solid solution fcc phase had formed along the grain boundaries. Although the phases present at this composition were the same as in the as built state, the homogenizing heat treatment induced substantial changes in the size, distribution, and composition of these phases. It is furthermore remarkable that this microstructure exhibited by far the highest hardness of all conditions analyzed.

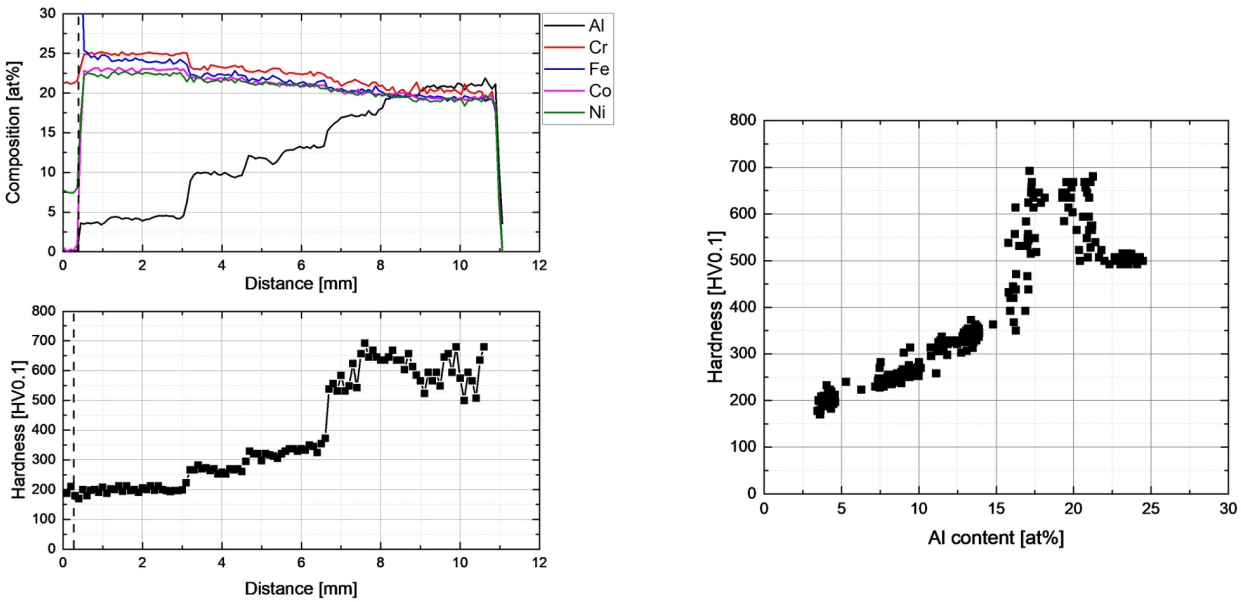

FIGURE 8 | Chemical composition and hardness of the 5/15/25 at% Al gradient structure after heat treatment (left); hardness as a function of Al content derived from all three heat treated gradients (right).

When the overall Al content exceeded 20 at%, as displayed by sample positions 5 and 6, the fcc phase completely vanished and the amount of the Al and Ni rich ordered bcc B2 phase strongly increased. Hence, the predominant phase at this high Al content was the ordered bcc B2 phase. Within this B2 matrix a rather fine and dense arrangement of mainly spherical bcc A2 particles was present. Due to the heat treatment the initially dendritic structure and the accompanying segregations completed vanished. Surprisingly, the hardness of the Al rich B2/A2 dual bcc structure (position 5 and 6) was considerably lower than the hardness of the complex fcc + A2 + B2 bcc structure at an intermediate Al content (position 4).

DISCUSSION

In order to validate thermodynamic calculations as well as effectively produce samples with varying chemical compositions and to build up material libraries for the HEA research, the use of laser and powder based additive manufacturing methods were suggested by Haase et al. (2017) and Li et al. (2018). By varying the powder composition and feed rate and mixing the different powders in situ in the process a wide range of HEA alloy composition can be created very rapidly. In our work this high throughput methodology for HEA alloy fabrication was further developed. By building up tracks that lay on top of each other the Al feed rate was changed every third layer in order to achieve a structure with a gradient in Al content. As a result within only one sample six different compositions of the $Al_xCoCrFeNi$ alloy system could be fabricated. Using this methodology the screening approach could be successfully extended from the alloy fabrication to the analysis of chemical composition, hardness, and structure as well. The obtained results are generally in good agreement with those reported in literature on individual additive manufactured samples while requiring significantly less time for fabrication and analyzing.

Studies on arc-melted and cast samples of $Al_xCoCrFeNi$ reported a transition from a fully fcc phase to a fully dual phase A2/B2 bcc structure in the range from about 10 at% to 19 at% Al content (Kao et al., 2009; Wang et al., 2012). Li et al. (2018) studying 21 different compositions in the $Al_xCoCrFeNi$ alloy system utilizing a laser based LENS process found a similar transition region between about 9 and 21 at%. In contrast, in our work applying LMD to synthesize different alloy compositions of $Al_xCoCrFeNi$, the phase transition occurred in the narrow range from about 10 to 15 at% overall Al content. With increasing Al contents beyond 15 at% only minor microstructural changes in the form of a beginning segregation into Al rich cores (bcc^*_d) and Fe – Cr rich interdendritic areas (bcc^*_{id}) were observed, resulting in a change in local B2/A2 phase fractions. It is proposed that the high laser induced cooling rate of 10^3–10^5 Ks^{-1} associated with the LMD process allowed for a so-called solute trapping that favors sample conditions far from thermal equilibrium and hence the observed phase formation behavior (Xiang et al., 2019). Even though the exact cooling rates of the casting and the LENS process were not given in literature, they were probably lower than for the LMD process. In the case of the casting process much higher melt volumes were involved than in the LMD process leading to lower cooling rates. On the other hand, the LENS process involved several remelting steps and therefore allowed structures closer to the thermal equilibrium compared to the LMD process in our work. The importance of cooling rate and thermal equilibrium to the phase transformation taking place in the $Al_xCoCrFeNi$ alloys system was confirmed

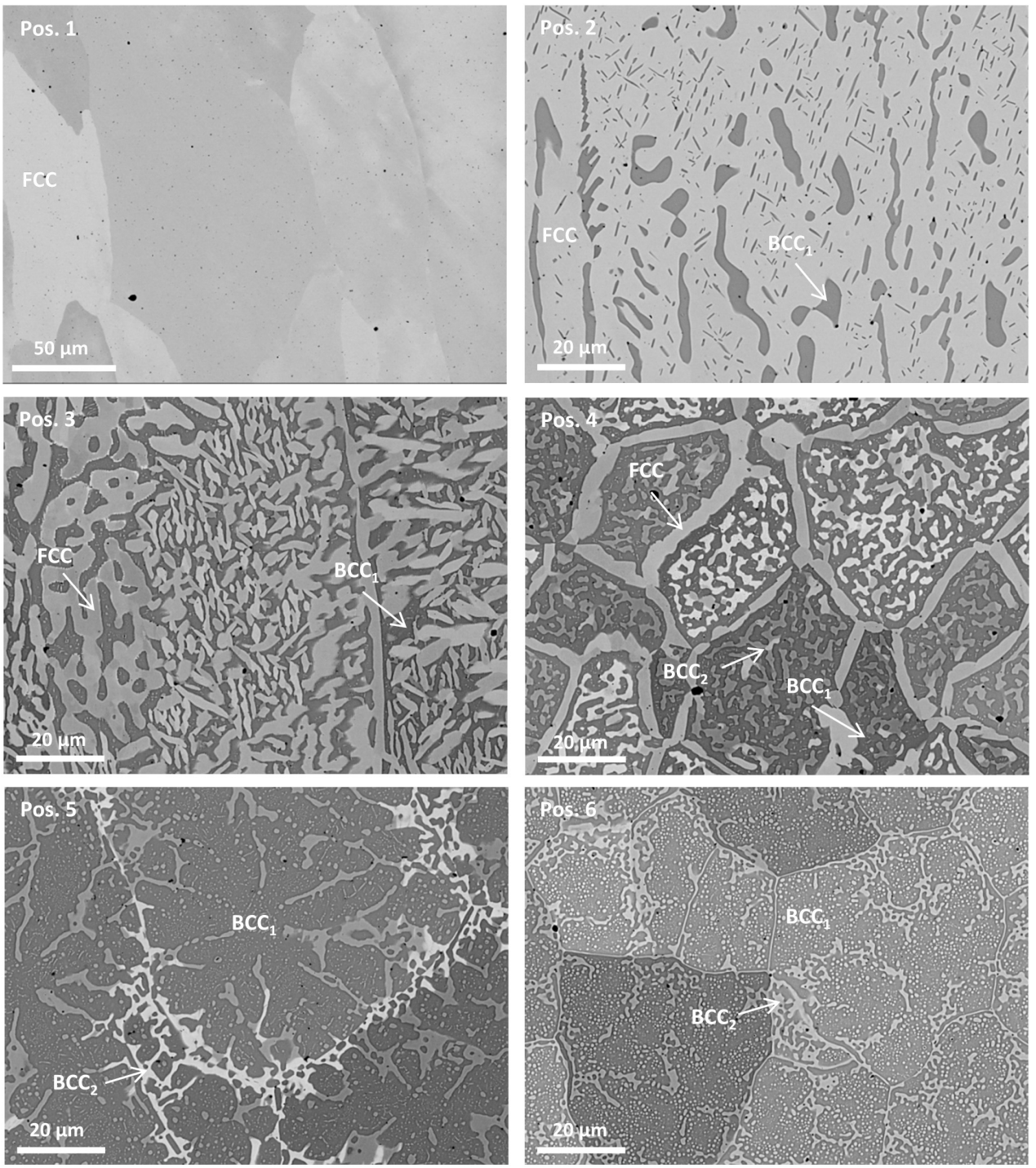

FIGURE 9 | SEM images of the major microstructures of the samples after heat treatment with increasing Al content derived from all three cladded gradients: Pos. 1 at 4.8 at.% Al, Pos. 2 at 10.4 at.% Al, Pos. 3 at 14.7 at.% Al, Pos. 4 at 17.5 at.% Al, Pos. 5 at 23.5 at.% Al, and Pos. 6 at 24.6 at.% Al.

by CALPHAD calculations in literature (Zhang et al., 2016; Butler and Weaver, 2017) and our own work (**Figure 1**). For thermal equilibrium conditions at homogenizing temperature these calculations predicted a very broad range from 5 to 20 at% Al content for the complete transition from fcc to bcc phases.

Another difference between the prediction of the CALPHAD calculations and the experimental results obtained from the LMD as built state regarding the structural evolution was recognized. According to the CALPHAD calculations the transition process from fcc to bcc initiated with the formation of only one

TABLE 4 | Representative EDS analysis of the major regions of the samples after heat treatment (at %).

Pos.	Area	Al	Cr	Fe	Co	Ni
1	Overall	4.8	24.3	23.8	23.8	23.3
	fcc	4.8	***24.3***	***23.8***	***23.8***	***23.3***
2	Overall	10.4	22.4	22.2	22.5	22.5
	fcc	5.9	***25.6***	***24.6***	***23.8***	20.1
	bcc1	***29.1***	7.5	11.6	17.1	***34.7***
3	Overall	14.7	21.2	21.1	21.4	21.6
	fcc	5.7	***27.8***	***27***	***23.3***	16.1
	bcc1	***28.2***	10.2	13.0	18.6	***30.1***
4	Overall	17.5	20.6	20.2	20.6	21.1
	fcc	5.3	***27.3***	***28.7***	***24.1***	14.6
	bcc1	***27.7***	9.0	13.8	20.0	***29.6***
	bcc2	3.4	***44.2***	***27.5***	18.7	6.2
5	Overall	23.5	18.0	18.4	19.8	20.3
	bcc1	***28.8***	10.6	15.2	20.8	***24.7***
	bcc2	4.0	***46.2***	***30.4***	15.1	4.3
6	Overall	24.6	19.5	18.8	18.8	18.3
	bcc1	***28.4***	14.2	16.5	19.8	***21.1***
	bcc2	7.6	***47.7***	***31.8***	10.0	2.9

The bold values indicate differences in phase composition.

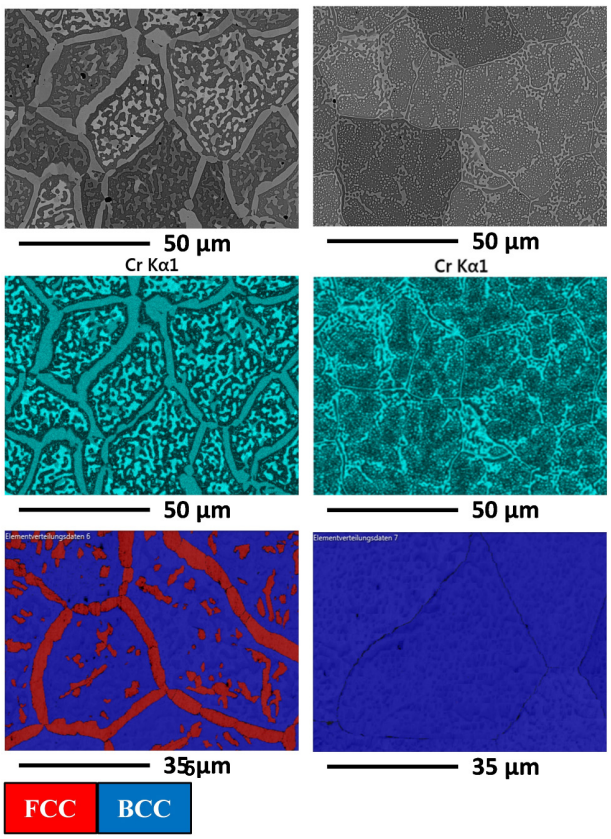

FIGURE 10 | EDS Cr maps and EBSD phase maps of sample positions 4 (left) and 6 (right).

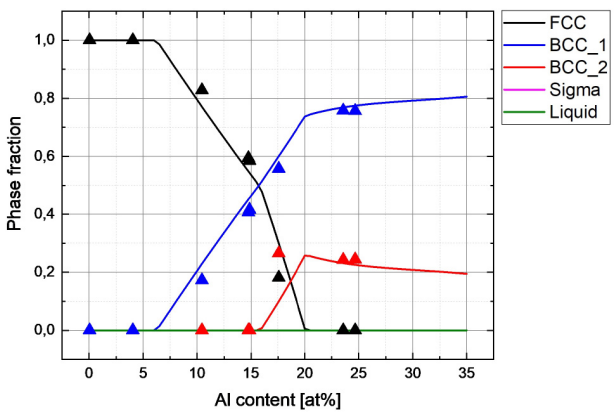

FIGURE 11 | Phase formation in the $Al_xCoCrFeNi$ alloy system homogenized at 1350 K in dependence on the Al content; lines: CALPHAD calculations, symbols: experimental data derived from structural analysis.

bcc phase (bcc1) at about 5 at% Al content. Not until an Al content of about 15 at% Al was exceeded a second bcc phase (bcc2) at a lower phase fraction was predicted. In accordance with Butler and Weaver (2017) bcc1 and bcc2 will be regarded as B2 and A2 phases, respectively. In the as built state of the LMD samples already with the first occurrence of the bcc phase at 10 at% Al the very fine-scaled dual B2/A2 phase arrangement denoted as bcc* formed. This was in contrast to the predictions of the CALPHAD calculations. Although the amount of bcc* increased with increasing Al content, the general appearance of this B2/A2 phase mixture remained unchanged. This is in good agreement with most of the experimental data in literature derived from melting and casting (Wang et al., 2012; Munitz et al., 2016; Lim et al., 2017; Meshi et al., 2019) as well as the additive manufacturing fabrication route (Kunce et al., 2015; Li et al., 2018; Niu et al., 2019; Karlsson et al., 2019b) of $Al_xCoCrFeNi$ alloys. In accordance with the interpretation of Li et al. (2018) and Karlsson et al. (2019b) the very fine-scaled dual B2/A2 phase arrangement is regarded as the result of a spinodal decomposition.

Previous works performed on equiatomic AlCoCrFeNi or near equiatomic $Al_{0.9}CoCrFeNi$ showed that these alloys underwent the following transformation of B2 + A2 → B2 + fcc (A1) + σ during heat treatment at 1123 K (Wang et al., 2014; Meshi et al., 2019). The formation of the brittle σ-phase in $Al_xCoCrFeNi$ alloys at intermediate temperatures has been regarded as a major drawback for industrial applications since it probably limits the operating temperatures to 500°C. According to CALPHAD calculations and the literature discussed in the introduction the avoidance of σ-phase formation during homogenization treatments require temperatures above approximately 1250 K at which the σ-phase dissolves leading to a mixture of A2 + B2 + fcc phases (Munitz et al., 2016; Butler and Weaver, 2017). In our work the homogenization temperature was chosen to be 1350 K, i.e., clearly above this critical temperature. In the range from 5 to 20 at% overall Al content our isothermal CALPHAD calculations at

1350 K predict a combination of fcc, B2, and/or A2 phase depending on the alloy composition (**Figure 1**). Exceeding an overall Al content of 5 at% the phase fraction of the B2 phase increased to the extent of the fcc phase. This prediction was confirmed by our experimental data from annealed LMD samples exhibiting 10.4 and 14.7 at% Al content (positions 2 and 3 in **Figure 9**). Also consistent with the CALPHAD calculations the A2 phase occurred at 17.5 at% Al content (position 4 in **Figure 9**) and the fcc phase completely disappeared at 23.5 and 24.6 at% Al content (position 5 and 6 in **Figure 9**). **Figure 11** visualizes the good agreement of the phase formation behavior of LMD synthesized and annealed $Al_xCoCrFeNi$ alloys with our CALPHAD calculations. A similar good agreement was found in literature with experimental data from vacuum arc-melted, cast and annealed $Al_xCoCrFeNi$ alloys (Butler and Weaver, 2017).

There is a pronounced hardness maximum in the LMD fabricated and annealed $Al_xCoCrFeNi$ alloys in the range from about 17 to about 23 at% overall Al content. At this maximum the hardness of the as built state at the same Al concentrations and also of homogenized samples at higher Al concentrations was exceeded by more than 200 HV. No such hardness maximum was yet reported in vacuum arc-melted, cast, and annealed samples (Kao et al., 2009; Wang et al., 2014). To the best of the authors' knowledge there is no structural and hardness data from additive manufactured and homogenized samples in literature so far to compare the given results with. It is remarkable, however, that the pronounced hardness maximum corresponds directly to the three phase region of fcc + B2 + A2. It is therefore proposed that these three phases arrange to a preferable compound that together with the accompanying grain and phase refinement contributes to this local hardness maximum. However, in order to fully understand the active hardening mechanisms, further structural analysis including TEM is necessary and will be the focus of future research activities.

CONCLUSION

In the present study an experimental methodology based on LMD that allows high throughput experimental screening of HEAs/CCAs including the fabrication and characterization process was introduced. Applying this procedure to the $Al_xCoCrFeNi$ alloy system compositions from 5 to 30 at% Al content were synthesized in gradient structures by LMD and the microstructure and hardness in the as built and homogenized state were investigated in detail. Based on these results the following conclusions were drawn:

(1) LMD utilizing in situ alloying of different pre-alloyed or elemental powders is a very powerful and reliable tool for high throughput screening, fabrication, and the alloy design of HEAs/CCAs.
(2) In the as built condition a microstructural change from single phase solid solution fcc to a fine scaled dual phase bcc microstructure (Fe-Cr rich solid solution bcc phase [A2] and Al-Ni rich ordered bcc phase [B2]) occurred in the narrow range between 10 and 15 at% overall Al content. This structural change correlates to an increase of sample hardness from about 200 to 500 HV. The observed phase formation behavior differs strongly from the CALPHAD calculations at thermal equilibrium. This is due to the typically high cooling rates well known for LMD which promote non-equilibrium conditions.
(3) In the homogenized state the transition from single phase solid solution fcc to ordered B2 phase and finally the dual phase bcc microstructure (B2/A2) occurs in a much wider range from 5 to 23 at% overall Al content. The phase formation and transformation behavior is in very good agreement with homogenized vacuum-arc melted samples and the CALPHAD calculations at thermal equilibrium.
(4) In the homogenized state the structural changes can be correlated to a change in hardness, as well. The maximum hardness of about 700 HV exceeds the hardness of the as built state by more than 200 HV. It is correlated with a favorable formation and arrangement of all three phases (fcc + B2 + A2) and the resulting grain refinement.
(5) The experimental and calculated results in this work demonstrate the effectiveness of CALPHAD methods for the prediction of phase formation in HEAs/CCAs even though a lot of the thermodynamic data from ternary and quaternary systems is still not available.
(6) The mechanical properties of the $Al_xCoCrFeNi$ alloy system can be tuned by the right composition, especially with respect to Al content and using an appropriate annealing heat treatment.

DATA AVAILABILITY STATEMENT

The raw data supporting the conclusions of this article will be made available by the authors, without undue reservation.

AUTHOR CONTRIBUTIONS

JK, MZ, and CL contributed to conception and design of the study. MK performed the CALPHAD calculations and most of the structural analysis. LK performed the cladding experiments by LMD. MK wrote the first draft of the manuscript. JK wrote sections of the manuscript. JK and MZ critically revised the manuscript. All authors read and approved the submitted version.

FUNDING

The research of the present work was supported by internal Fraunhofer funding. Furthermore the financial support from the Federal Ministry for Economic Affairs and Energy in Germany within the "Central Innovation Program for small and medium-sized enterprises (ZIM funding)," Funding code: 16KN081123 is gratefully acknowledged.

REFERENCES

Brueckner, F., Riede, M., Müller, M., Marquardt, F., Willner, R., Seidel, A., et al. (2018). Enhanced manufacturing possibilities using multi-materials in laser metal deposition. *J. Laser Applic.* 30, 1–8. doi: 10.2351/1.5040639

Butler, T. M., and Weaver, M. L. (2017). Investigation of the phase stabilities in AlNiCoCrFe high entropy alloys. *J. Alloys Comp.* 691, 119–129. doi: 10.1016/j.jallcom.2016.08.121

Cantor, B., Chang, I. T. H., Knight, P., and Vincent, A. J. B. (2004). Microstructural development in equiatomic multicomponent alloys. *Mater. Sci. Eng. A* 375-377, 213–218. doi: 10.1016/j.msea.2003.10.257

Fujieda, T., Shiratori, H., Kuwabara, K., Kato, T., Yamanaka, K., Koizumi, Y., et al. (2015). First demonstration of promising selective electron beam melting method for utilizing high-entropy alloys as engineering materials. *Mater. Lett.* 159, 12–15. doi: 10.1016/j.matlet.2015.06.046

Gwalani, B., Gangireddy, S., Shukla, S., Yannetta, C. J., Valentin, S. G., Mishra, R. S., et al. (2019). Compositionally graded high entropy alloy with a strong front and ductile back. *Mater. Today Commun.* 20:100602. doi: 10.1016/j.mtcomm.2019.100602

Haase, C., Tang, F., Wilms, M. B., Weisheit, A., and Hallstedt, B. (2017). Combining thermodynamic modeling and 3D printing of elemental powder blends for high-throughput investigation of high-entropy alloys – Towards rapid alloy screening and design. *Mater. Sci. Eng. A* 688, 180–189. doi: 10.1016/j.msea.2017.01.099

Kao, Y. F., Chen, T. J., Chen, S. K., and Yeh, J. W. (2009). Microstructure and mechanical property of as-cast, -homogenized, and -deformed AlxCoCrFeNi ($0 \leq x \leq 2$) high-entropy alloys. *J. Alloys Comp.* 488, 57–64. doi: 10.1016/j.jallcom.2009.08.090

Karlsson, D., Lindwall, G., Lundbäck, A., Amnebrink, M., Boström, M., Riekehr, L., et al. (2019a). Binder jetting of the AlCoCrFeNi alloy. *Addit. Manuf.* 27, 72–79. doi: 10.1016/j.addma.2019.02.010

Karlsson, D., Marshal, A., Johansson, F., Schuisky, M., Sahlberg, M., Schneider, J. M., et al. (2019b). Elemental segregation in an AlCoCrFeNi high-entropy alloy – A comparison between selective laser melting and induction melting. *J. Alloys Comp.* 784, 195–203. doi: 10.1016/j.jallcom.2018.12.267

Kunce, I., Polanski, M., Karczewski, K., Plocinski, T., and Kurzydlowski, K. J. (2015). Microstructural characterisation of high-entropy alloy AlCoCrFeNi fabricated by laser engineered net shaping. *J. Alloys Comp.* 648, 751–758. doi: 10.1016/j.jallcom.2015.05.144

Kuwabara, K., Shiratori, H., Fujieda, T., Yamanaka, K., Koizumi, Y., and Chiba, A. (2018). Mechanical and corrosion properties of AlCoCrFeNi high-entropy alloy fabricated with selective electron beam melting. *Addit. Manuf.* 23, 264–271. doi: 10.1016/j.addma.2018.06.006

Leino, M., Pekkarinen, J., and Soukka, R. (2016). The role of laser additive manufacturing methods of metals in repair, refurbishment and remanufacturing – enabling circular economy. *Phys. Proc.* 83, 752–760. doi: 10.1016/j.phpro.2016.08.077

Li, M., Gazquez, J., Borisevich, A., Mishra, R., and Flores, K. M. (2018). Evaluation of microstructure and mechanical property variations in Al x CoCrFeNi high entropy alloys produced by a high-throughput laser deposition method. *Intermetallics* 95, 110–118. doi: 10.1016/j.intermet.2018.01.021

Lim, K. R., Lee, K. S., Lee, J. S., Kim, J. Y., Chang, H. J., and Na, Y. S. (2017). Dual-phase high-entropy alloys for high-temperature structural applications. *J. Alloys Comp.* 728, 1235–1238. doi: 10.1016/j.jallcom.2017.09.089

Manzoni, A., Daoud, H., Völkl, R., Glatzel, U., and Wanderka, N. (2013). Phase separation in equiatomic AlCoCrFeNi high-entropy alloy. *Ultramicroscopy* 132, 212–215. doi: 10.1016/j.ultramic.2012.12.015

Marshal, A., Pradeep, K. G., Music, D., Zaefferer, S., De, P. S., and Schneider, J. M. (2017). Combinatorial synthesis of high entropy alloys: introduction of a novel, single phase, body-centered-cubic FeMnCoCrAl solid solution. *J. Alloys Comp.* 691, 683–689. doi: 10.1016/j.jallcom.2016.08.326

Meshi, L., Linden, Y., Munitz, A., Salhov, S., and Pinkas, M. (2019). Retardation of the σ phase formation in the AlCoCrFeNi multi-component alloy. *Mater. Characterization* 148, 171–177. doi: 10.1016/j.matchar.2018.12.010

Miracle, D. B., and Senkov, O. N. (2017). A critical review of high entropy alloys and related concepts. *Acta Mater.* 112, 448–511. doi: 10.1016/j.actamat.2016.08.081

Mohanty, A., Sampreeth, J. K., Bembalge, O., Hascoet, J. Y., Marya, S., Immanuel, R. J., et al. (2019). High temperature oxidation study of direct laser deposited AlXCoCrFeNi (X = 0.3,0.7) high entropy alloys. *Surface Coat. Technol.* 380:125028. doi: 10.1016/j.surfcoat.2019.125028

Munitz, A., Salhov, S., Hayun, S., and Frage, N. (2016). Heat treatment impacts the micro-structure and mechanical properties of AlCoCrFeNi high entropy alloy. *J. Alloys Comp.* 683, 221–230. doi: 10.1016/j.jallcom.2016.05.034

Niu, P. D., Li, R. D., Yuan, T. C., Zhu, S. Y., Chen, C., Wang, M. B., et al. (2019). Microstructures and properties of an equimolar AlCoCrFeNi high entropy alloy printed by selective laser melting. *Intermetallics* 104, 24–32. doi: 10.1016/j.intermet.2018.10.018

Shiratori, H., Fujieda, T., Yamanaka, K., Koizumi, Y., Kuwabara, K., Kato, T., et al. (2016). Relationship between the microstructure and mechanical properties of an equiatomic AlCoCrFeNi high-entropy alloy fabricated by selective electron beam melting. *Mater. Sci. Eng. A* 656, 39–46. doi: 10.1016/j.msea.2016.01.019

Wang, R., Zhang, K., Davies, C., and Wu, X. (2017). Evolution of microstructure, mechanical and corrosion properties of AlCoCrFeNi high-entropy alloy prepared by direct laser fabrication. *J. Alloys Comp.* 694, 971–981. doi: 10.1016/j.jallcom.2016.10.138

Wang, W. R., Wang, W. L., Wang, S. C., Tsai, Y. C., Lai, C. H., and Yeh, J. W. (2012). Effects of Al addition on the microstructure and mechanical property of AlxCoCrFeNi high-entropy alloys. *Intermetallics* 26, 44–51. doi: 10.1016/j.intermet.2012.03.005

Wang, W. R., Wang, W. L., and Yeh, J. W. (2014). Phases, microstructure and mechanical properties of AlxCoCrFeNi high-entropy alloys at elevated temperatures. *J. Alloys Comp.* 589, 143–152. doi: 10.1016/j.jallcom.2013.11.084

Xiang, S., Luan, H., Wu, J., Yao, K. F., Li, J., Liu, X., et al. (2019). Microstructures and mechanical properties of CrMnFeCoNi high entropy alloys fabricated using laser metal deposition technique. *J. Alloys Comp.* 773, 387–392. doi: 10.1016/j.jallcom.2018.09.235

Yeh, J. W., Chen, S. K., Lin, S. J., Gan, J. Y., Chin, T. S., Shun, T. T., et al. (2004). Nanostructured high-entropy alloys with multiple principal elements: novel alloy design concepts and outcomes // nanostructured high-entropy alloys with multiple principal elements: novel alloy design concepts and outcomes. *Adv. Eng. Mater.* 6, 299–303. doi: 10.1002/adem.200300567

Zhang, C., Zhang, F., Diao, H., Gao, M. C., Tang, Z., Poplawsky, J. D., et al. (2016). Understanding phase stability of Al-Co-Cr-Fe-Ni high entropy alloys. *Mater. Des.* 109, 425–433. doi: 10.1016/j.matdes.2016.07.073

Conflict of Interest: The authors declare that the research was conducted in the absence of any commercial or financial relationships that could be construed as a potential conflict of interest.